SIZE AND STRUCTURE OF ANTIGEN–ANTIBODY COMPLEXES

Electron Microscopy and Light Scattering Studies

REGINA M. MURPHY,* HENRY SLAYTER,§ PETER SCHURTENBERGER,‡
RICHARD A. CHAMBERLIN,‡ CLARK K. COLTON,* AND MARTIN L. YARMUSH*
**Department of Chemical Engineering and ‡Department of Physics and Center for Materials Science and Engineering, Massachusetts Institute of Technology, Cambridge, Massachusetts 02139; and §Dana Farber Cancer Institute and Department of Biophysics and Physiology, Harvard Medical School, Boston, Massachusetts 02115*

ABSTRACT Size parameters of model antigen–antibody (Ag-Ab) complexes formed by the interaction of bovine serum albumin (BSA) and pairs of monoclonal anti-BSA antibodies (mAb) were evaluated by quasielastic light scattering, classical light scattering, and electron microscopy (EM). Mean values for the hydrodynamic radius, radius of gyration, and molecular weight were determined by light scattering. Detailed information regarding the molecular weight distribution and the presence of cycles or open chains was obtained with EM. Average molecular weights were calculated from the EM data, and the Porod-Kratky wormlike chain theory was used to model the conformational behavior of the Ag-mAb complexes. Ag-mAb complexes prepared from three different mAb pairs displayed significantly different properties as assessed by each of the techniques employed. Observations and size parameter calculations from EM photomicrographs were consistent with the results from light scattering. The differences observed between the mab pairs would not have been predicted by idealized thermodynamic models. These results suggest that the geometric constraints imposed by the individual epitope environment and/or the relative epitope location are important in determining the average size of complexes and the ratio of linear to cyclic complexes.

INTRODUCTION

The interaction of antigen (Ag) and antibody (Ab) results in the formation of Ag-Ab complexes. These interactions are noncovalent and depend mainly on the structural complementarity between the three-dimensional surfaces of the Ag molecule and the Ab binding site. Many physiological properties of soluble Ag-Ab complexes, including clearance from the circulation, complement fixation, adherence to phagocytes, and differential tissue deposition, depend on the size and composition of these complexes (1–4). Much of the early work on determination of size and composition of Ag-Ab complexes was performed with polyclonal antibodies (5, 6). However, a detailed quantitative picture was difficult to obtain with polyclonal systems because of the heterogeneity involved. More recently, Steensgard and co-workers have used monoclonal antibodies (mAb) with defined characteristics to generate Ag-mAb complexes (7). Yet experimental results in simple systems with well-characterized mAb were found at times to deviate from results predicted by idealized thermodynamic models.

In a previous paper (8), we described experiments in which the hydrodynamic radius of Ag-mAb complexes of bovine serum albumin (BSA) and two or three anti-BSA mAb at varying molar ratios and concentrations was measured using quasielastic light scattering. The present report describes a more detailed characterization of the mean size and size distribution of the model complexes containing two mAb. Ag-mAb complex size was evaluated experimentally by both classical and quasielastic light scattering. Size distributions were examined by electron microscopy. Molecular weight and size parameters evaluated by the different techniques were comparable. The results suggest that the geometric constraints imposed by the individual epitope environment and/or the relative epitope location are important in determining the average size of complexes and the ratio of linear to cyclic complexes.

MATERIALS AND METHODS

Bovine Serum Albumin (BSA)

BSA (globulin-free, Sigma Chemical Co., St. Louis, MO) was dissolved in phosphate-buffered saline (PBSA: 0.15 M NaCl, 0.01 M KH_2PO_4/K_2HPO_4, 0.02% [wt/vol] sodium azide, pH 7.0), purified by gel perme-

Address correspondence to Martin L. Yarmush.

ation chromatography on a Sephadex G-150 (Pharmacia Fine Chemicals, Piscataway, NJ) column to remove oligomers, and concentrated in a stirred ultrafiltration cell with a YM-10 membrane (Amicon, Danvers, MA). The extinction coefficient (0.60 ml/mg · cm) was determined by dialyzing BSA against water extensively to remove salts, then lyophilizing, weighing the powder, dissolving the powder in a known volume of PBSA, and measuring the optical density at 280 nm (model DU-50 spectrophotometer, Beckman Instruments, Inc., Somerset, NJ). Concentrations of unknown samples were determined by optical density measurement at 280 nm.

Monoclonal Antibodies (mAb)

Three anti-BSA mAb were selected from a panel of 12 mAb which had been characterized in detail (9) (Table I). The three mAb bind noncompetitively to three different BSA subdomains (10). The mAb were prepared from hybridoma cell lines designated as 5.1, 6.1, and 9.1. Cells were injected intraperitoneally into pristane-primed nude mice. Ascites fluid was tapped 10–20 d after injection, centrifuged to discard cells, and stored at −70°C. mAb was isolated from aliquots of thawed ascites fluid by immunoadsorption using a column of Sepharose CL-4B (Pharmacia Fine Chemicals) to which BSA was covalently linked via activation with 1-cyano-4-(dimethylamino)-pyridinium tetrafluoroborate (11). mAb was eluted with 0.1 M glycine/HCl buffer, pH 2.5, dialyzed against PBSA, concentrated by ultrafiltration on an Amicon YM-30 membrane, and chromatographed on a Sephadex G-200 column to remove oligomers. Fractions corresponding to monomer IgG were collected and concentrated again by ultrafiltration. Concentration was determined by optical density measurement at 280 nm, using measured extinction coefficients of 1.5, 1.45, and 1.7 ml/mg · cm for mAb 5.1, 6.1, and 9.1, respectively. Equilibrium association constants of the purified mAb were determined by radioimmunoassay as described previously (9) and were consistent from batch to batch. Stock solutions were routinely checked for aggregation by quasielastic light scattering before use.

Light Scattering

The classical light scattering (CLS) and quasielastic light scattering (QLS) experiments were performed on a light scattering photometer resembling the instrument described by Haller et al. (12). Scattered light from a sample was detected at 12 fixed angles spaced equally in $\log_{10}q$, where $q = (4\pi n/\lambda_0) \sin(\theta/2)$ is the scattering vector, n is the refractive index of the solvent (1.33 for PBSA), λ_0 is the wavelength of incident light in vacuo, and θ is the scattering angle, which ranged from 11.5 to 162.6°. A vertically polarized argon-ion laser (model 90-5, Coherent Inc., Palo Alto, CA) operating at $\lambda_0 = 488$ nm and ~100 mW was used as the light source. Computer-controlled solenoid-actuated shutters were used to select one of the 12 scattering angles or the attenuated transmitted laser beam for measurement. The collected light was guided from the shutters to a single photomultiplier tube (model 9863A-100, EMI, Hayes, UK) by 1-mm diameter optical fibers (model HC-1006-T, Ensign-Bickford, Avon, CT). A dust-free water bath provided temperature control and refractive index matching to the sample glass cell. The sample was maintained at 20.00 ± 0.01°C.

TABLE I
CHARACTERISTICS OF MONOCLONAL ANTIBODIES

mAb	Association constant $K_a(M^{-1})$	Subdomain*	Isoelectric point	Isotype
	M^{-1}			
5.1	24×10^7	1-C	8.9–9.1	$\gamma 1, \kappa$
6.1	3.6×10^7	1-N	7.6–7.7	$\gamma 1, \kappa$
9.1	20×10^7	3-C	6.9–7.1	$\gamma 1, \kappa$

*BSA fragment to which the mAb binds, determined by enzyme-linked immunoassay using BSA fragments (9).

Samples were prepared by dilution of stock solutions of mAb and BSA with PBSA to a BSA concentration of 8.25×10^{-7} M and a mAb_1:mAb_2:BSA molar ratio of 0.45:0.45:1. This ratio yielded roughly a maximum mean size, for a given Ag concentration, as measured by QLS (8). Absorbance of the samples at 280 nm was measured before and after light scattering experiments to check that no change in concentration occurred due to filtration or adsorption. 8 ml of solution were then transferred into a cylindrical glass cell (30 mm inner diameter × 32 mm outer diameter × 60 mm height). The cell was sealed and the solution was filtered through a closed-loop system using a Millex GV 0.22-μm filter (Millipore, Bedford, MA) until telescopic inspection of the scattered light at 17.4° showed the sample to be free of dust.

For classical light scattering measurements, the intensity of the transmitted laser beam I_0 and the intensity of the light scattered at 12 angles $I(\theta)$ were sequentially sampled 50–100 times and stored on a computer (DEC Pro 350, Digital Equipment Corp., Maynard, MA) for further data reduction and analysis. The values for $I(\theta)$ were then normalized with respect to I_0 and averaged using a dust discrimination procedure (12). This data reduction scheme reduced inaccuracies due to drifts in laser power and/or photomultiplier response and automatically corrected $I(\theta)$ for sample turbidity. The background stray light and solvent contributions $I_b(\theta)$ were then measured using the same cell containing highly purified and filtered water and subtracted from $I(\theta)$. The resulting intensity data were then normalized with respect to intensity data $I_r(\theta)$ from a pure, isotropically scattering reference solvent with known Rayleigh ratio $R_r(\theta)$ to correct for instrument response differences at each angle. Toluene (spectrophotometric grade, Aldrich Chemical Co., Milwaukee, WI) was used as a reference solvent, and the Rayleigh ratio of the sample $R_s(\theta)$ was calculated from

$$R_s(\theta) = \frac{I_s(\theta) - I_b(\theta)}{I_r(\theta)} R_r(\theta) \left(\frac{n}{n_r}\right)^2, \quad (1)$$

where n and n_r are the index of refraction of the sample solvent and the reference solvent, respectively. The factor $(n/n_r)^2$ corrects for the change of scattering volume and acceptance solid angle with changing index of refraction. The Rayleigh ratio of toluene $R_r(\theta)$ was taken to be $39.6 \times 10^{-4}\ m^{-1}$ (13).

Light scattering from solutions of macromolecules is commonly represented by (14)

$$\frac{Kc}{R_s(\theta)} = \frac{1}{P(\theta)\langle M \rangle_w} + 2Bc + \cdots, \quad (2)$$

where $K = 4\pi^2 n^2 (dn/dc)^2 / N_A \lambda_0^4$, dn/dc is the refractive index increment, c is concentration in mg/ml, $P(\theta)$ is a particle scattering factor, $\langle M \rangle_w$ is the weight-average molecular weight of the particles in solution, and B is the second viral coefficient. At low concentrations and small particle size relative to the wavelength of the incident beam, Eq. 2 can be simplified to (14):

$$\frac{Kc}{R_s(\theta)} = \frac{1}{\langle M \rangle_w} \left(1 + \frac{1}{3} q^2 \langle R_g^2 \rangle_z\right), \quad (3)$$

where $\langle R_g^2 \rangle_z$ is the z-average mean-square radius of gyration. Eq. 3 was used to fit light-scattering data. No correction for anisotropic scattering was made because of the generally low depolarization ratio of proteins (14).

For the determination of dn/dc, solutions of BSA, mAb, and mAb plus BSA were made up at varying concentrations. The optical density was measured at 280 nm and the concentration calculated using the measured extinction coefficients. The refractive index of the solution was measured using an Abbe 3-L refractometer (Bausch and Lomb Inc., Rochester, NY). The temperature of the refractometer was controlled to 20 ± 0.5°C by a circulating water bath. The refractometer calibration was checked

using NaCl solutions. A value of 0.19 ml/mg was obtained for dn/dc, consistent with literature values for BSA and human gammaglobulin (15).

Quasielastic light scattering measurements were made using the same instrument at five different angles (14.5, 23, 36.9, 60.2, and 90°). In these experiments, the shutter at a single angle was held open and photocounts were fed into a model 1096 correlator (Langley-Ford Instruments, Hialeah, FL). The method of cumulants (16) was used to fit the normalized autocorrelation function $|g^{(1)}(\tau)|$ to an equation of the form

$$ln|g^{(1)}(\tau)| = -\langle\Gamma\rangle\,\tau + \tfrac{1}{2}\mu_2\tau^2, \quad (4)$$

where $\langle\Gamma\rangle$ is the first cumulant, μ_2 is the variance, and τ is the autocorrelation delay time.

The first cumulant $\langle\Gamma\rangle$ can be expressed as (17)

$$\frac{\langle\Gamma\rangle}{q^2} = \langle D\rangle_z(1 + Cq^2\langle R_g^2\rangle_z + \cdots), \quad (5)$$

where $\langle D\rangle_z$ is the z-average translational diffusion coefficient, and C depends on molecular shape and polydispersity. The reciprocal of the z-average inverse hydrodynamic radius, denoted by $\langle R_h\rangle_z$, was then calculated from the Stokes-Einstein equation:

$$\langle R_h\rangle_z = \frac{kT}{6\pi\eta\langle D\rangle_z}, \quad (6)$$

where k is Boltzmann's constant, T is the absolute temperature, and η is the solvent viscosity.

Electron Microscopy

Samples of Ag-Ab complexes, at a BSA concentration of 1.65×10^{-6} M and a mAb_1:mAb_2:BSA molar ratio of 0.45:0.45:1.0, were made up in PBSA and dialyzed extensively against 0.15 M ammonium acetate, pH 6.8. The Ag-Ab complex solution was diluted to one-half its original concentration with glycerol, sprayed on to freshly cleaved mica, dried in vacuo, and rotary-shadowed with tungsten by means of electron-bombardment heating (18). In one case, a negative staining technique was used, in which the solution was dialyzed against 0.1 M Tris-HCl, pH 6.9, and uranyl acetate was added to a final concentration of 1% (wt/vol). The estimated average metal-film mass thickness was 10^{-7} g/cm^2. Samples were examined in a JEM 100 cx electron microscope, using a top-entry stage with a 40-μm objective aperture and a 100-kV acceleration voltage. Micrographs were recorded at a magnification of 40,000× and enlarged photographically to 128,000×. High-resolution dark-field images were obtained from these lightly shadowed specimens by using matched annular condenser and objective apertures. Photomicrographs were analyzed as follows. Individual monomers and complexes were identified, the number of units in each complex was counted, and the dimensions of each complex (contour length, end-to-end distance) were measured using a digital image analyzer (Laboratory Computer Systems Inc., Cambridge, MA). The complexes were identified visually as open linear chains or closed cycles. Complexes which were not clearly defined or did not appear as linear or cyclic structures were not selected for analysis. The sampling error incurred in counting a limited number of complexes belonging to a larger population was estimated using the De Moivre-Laplace Theorem (19). The true probability that any given complex contains i units is p_i. The probability P that the measured number N_i differs from the true number np_i by no more than a constant b times the product $[np_i(1 - p_i)]^{1/2}$ is given by

$$\lim_{n\to\infty} P\left(\left|\frac{N_i - np_i}{[np_i(1-p_i)]^{1/2}}\right| \leq b\right) \simeq \frac{1}{(2\pi)^{1/2}}\int_{-b}^{b} e^{-x^2/2}\,dx, \quad (7)$$

where $n = \Sigma N_i$ is the total number of all complexes, and the right hand side is evaluated from the normal probability distribution. The parameter b was chosen to give the desired probability P, p_i was approximated as N_i/n in the denominator, and $|N_i - np_i|$ was evaluated in the numerator, yielding an estimate of the sampling error within a prescribed confidence limit for each group of complexes of i units.

RESULTS

Light Scattering

Characteristics of mAb selected for these experiments are shown in Table I. Results for the three solutions are plotted in Fig. 1 as $\langle\Gamma\rangle/q^2$ vs. q^2. The intercept at $q^2 = 0$ yielded $\langle D\rangle_z$, which was then converted to an equivalent hydrodynamic radius $\langle R_h\rangle_z$ using Eq. 6. Values for $\langle R_h\rangle_z$ were markedly different for each of the three solutions. Values of $\langle D\rangle_z$ and $\langle R_h\rangle_z$ are listed in Table II.

To further characterize the size and shape of these complexes, classical light scattering experiments were carried out using the same solutions. The data are plotted in Fig. 2 as $(Kc/R_s(\theta))$ vs. q^2. The linearity of the fit supports the approximation of the particle scattering factor $P(\theta)$ used in Eq. 3. The average radius of gyration $\langle R_g^2\rangle_z^{1/2}$ was estimated by a weighted least-squares fit of the data to Eq. 3; results are listed in Table II. The substantially greater uncertainty in $\langle R_g^2\rangle_z^{1/2}$ than in $\langle R_h\rangle_z$ arises from the weak angular dependence with particles in this size range.

The weight-average molecular weight $\langle M\rangle_w$ was determined from the intercept in Fig. 2 using Eq. 3, and the results are summarized in Table III. Neglect of the third term ($2Bc$) in Eq. 2 introduces an error of <1%, based on calculations of the second virial coefficient from excluded volume estimates (20).

The differences in $\langle M\rangle_w$, $\langle R_h\rangle_z$, $\langle R_g^2\rangle_z^{1/2}$, and $\langle R_h\rangle_z/\langle R_g^2\rangle_z^{1/2}$ for the three solutions suggest that the size and/or shapes of the Ag-Ab complexes are different and that these differences cannot be attributed solely to differences in binding constants, because predictions of mean size parameters based upon the magnitudes of association constants

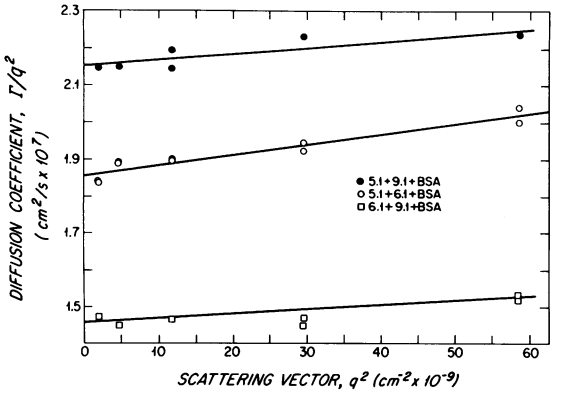

FIGURE 1 Dependence of $\langle\Gamma\rangle/q^2$ on q^2 for three different solutions, each containing 2 mAb + BSA. All three solutions were prepared in PBSA at a BSA concentration of 8.25×10^{-7} M and a mAb_1:mAb_2:Ag molar ratio of 0.45:0.45:1.0. Extrapolation to $q^2 = 0$ gives the true z-average translational diffusion coefficient $\langle D\rangle_z$. Symbols are data points; solid lines represent linear regression fits through all points.

TABLE II
DIFFUSION AND SIZE PARAMETERS OF Ag-mAb COMPLEXES

Components	Diffusion coefficient from QLS	Hydrodynamic radius from QLS	Radius of gyration from CLS	$\langle R_h \rangle_z / \langle R_g^2 \rangle_z^{1/2}$	Radius of gyration from EM
	$\langle D \rangle_z$, $cm^2/s \times 10^7$	$\langle R_h \rangle_z$, Å	$\langle R_g^2 \rangle_z^{1/2}$, Å		$\langle R_g^2 \rangle_z^{1/2}$, Å
5.1 + 9.1 + BSA	2.15 ± 0.04	99 ± 2	114 ± 19	0.87 ± 0.15	145 ± 13
5.1 + 6.1 + BSA	1.86 ± 0.02	114 ± 1	186 ± 23	0.61 ± 0.08	194 ± 16
6.1 + 9.1 + BSA	1.46 ± 0.02	146 ± 3	201 ± 15	0.73 ± 0.06	237 ± 27

Solutions were prepared at a BSA concentration of 8.25×10^{-7} and a mAb_1:mAb_2:BSA molar ratio of 0.45:0.45:1.0. All measurements are tabulated as fitted value ± estimated SD.

alone would show 5.1 + 9.1 to be larger than 6.1 + 9.1. To obtain additional information about size distribution and conformation of the complexes, each combination of two mAb + BSA was examined by electron microscopy.

Electron Microscopy

Representative electron micrographs are shown in Fig. 3. Individual antibodies appear as small triangles in rotary-shadowed specimens (21). Monomeric BSA is difficult to positively identify (22). Fig. 3 *A* (5.1 + 9.1) contains some single-antibody structures, many small, two-antibody cyclic structures, and a few longer linear chains. Fig. 3 *B* (5.1 + 6.1), in contrast, contains a number of single-antibody complexes, very few cycles, and a few longer linear chains. Fig. 3 *C* (6.1 + 9.1) shows a broader distribution in complex size, with many single-antibody complexes, very few two-antibody cycles, but some larger four-and six-antibody cycles and a number of long linear chains. In a control experiment with 9.1 + BSA, no cycles were observed, but a few linear chains apparently containing two or more antibodies were present.

Analysis of the photomicrographs included measurement, for each complex, of the contour length, the number of units in each complex, and the end-to-end distance (for each linear complex). The mean square end-to-end distance $\langle R^2 \rangle_i$ was calculated by squaring the measurement for each complex with i units and then averaging over all complexes containing i units. The results are summarized in Table IV.

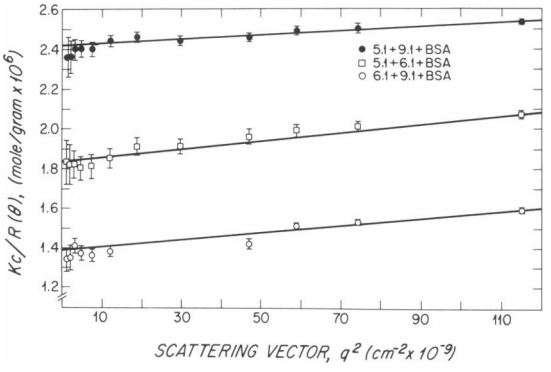

FIGURE 2 $Kc/R_s(\theta)$ plotted as a function of q^2. All three solutions were prepared in PBSA at a BSA concentration of 8.25×10^{-7} M and a mAb_1:mAb_2:Ag molar ratio of 0.45:0.45:1.0. The slope equals $\langle R_g^2 \rangle_z/3 \langle M \rangle_w$ and the intercept is $\langle M \rangle_w^{-1}$. Symbols represent an average of 50 to 100 measurements and error bars indicate the SD of these measurements. Solid lines are least-squares fits through the points, each weighted by the inverse of its variance.

The average contour length L_i as a function of the number of antibodies in the complex is plotted in Fig. 4. The average length of a unit was calculated by dividing the average contour length L_i for all complexes with i units (Table IV) by the number of units i in the complex and then averaging this over all complex sizes. The length (mean ± SD) for a unit was 190 ± 15 Å for 5.1 + 9.1, 201 ± 22 Å for 5.1 + 6.1, and 205 ± 26 Å for 6.1 + 9.1. The average length of a unit should correspond to the distance across the Y-extension of the antibody plus the length of BSA.

Number distributions of Ag-Ab complexes were determined from analysis of the micrographs by counting the number of complexes N_i containing a given number of units i and dividing by the total number n of all complexes; n was 409, 957, and 529 for the mAb pairs 5.1 + 6.1, 5.1 + 9.1, and 6.1 + 9.1, respectively. Histograms are plotted in Fig. 5 in terms of the fraction of the total number of complexes ($f_i = N_i/n$) vs. i. For $i = 2$, 4, and 6, the number of open and cyclic complexes is plotted separately. The frequency distributions reflect the qualitative observations made from the photomicrographs. These include a much higher fraction of two-and four-antibody cycles with 5.1 + 9.1 as compared with 5.1 + 6.1, comparable fractions of four- and six-antibody cycles with 5.1 + 9.1 and 6.1 + 9.1, and a higher fraction of longer ($i \geqq 5$) linear chains with 6.1 + 9.1 than with the other two.

Average molecular weights were calculated using the data in Table IV from

$$\langle M \rangle_n = \frac{\Sigma N_i M_i}{\Sigma N_i} \tag{8}$$

$$\langle M \rangle_w = \frac{\Sigma N_i M_i^2}{\Sigma N_i M_i} \tag{9}$$

$$\langle M \rangle_z = \frac{\Sigma N_i M_i^3}{\Sigma N_i M_i^2}, \tag{10}$$

TABLE III
MOLECULAR WEIGHTS OF Ag-Ab COMPLEXES

Components*	$10^3\langle M\rangle_w$, CLS	$10^3\langle M\rangle_w$, EM	$10^3\langle M\rangle_n$, EM	$10^3\langle M\rangle_z$, EM
5.1 + 9.1 + BSA	414 ± 34‡	568 ± 53§	427 ± 23	765 ± 101
5.1 + 6.1 + BSA	544 ± 41	573 ± 73	399 ± 33	783 ± 137
6.1 + 9.1 + BSA	721 ± 41	748 ± 28	482 ± 32	1,015 ± 149

*Solutions were prepared at a BSA concentration of 8.25×10^{-7} M and a mAb_1:mAb_2: BSA molar ratio of 0.45:0.45:1.0. ‡Estimated SD from a propagation of error analysis, which included the estimated error in the intercept from the weighted least-squares analysis of the CLS data (Fig. 2), the experimentally measured SD of ($R_s(\theta)$) and the assumptions that the concentration c was accurate to within ±0.01 mg/ml and the specific refractive index increment dn/dc was accurate within ±0.005 ml/mg. §Estimated SD from a propagation of error analysis using data in Table IV; SD of N_i was calculated from Eq. 7 with $b = 1.0$, and the SD in M_i was assumed to be ±35,000 (approximately one-half of the BSA molecule).

where M_i is the molecular weight of a complex with i units (Table IV), and $\langle M\rangle_n$, $\langle M\rangle_w$, and $\langle M\rangle_z$ are the number-average, weight-average, and z-average molecular weights, respectively. To estimate M_i, the molecular weight of a single Ag-mAb unit was approximated as 220,000 from the combined molecular weights of mouse IgG (153,000) and BSA (66,700) (23). $\langle M\rangle_w$, estimated from Eq. 9, was 568,000 ± 53,000, 573,000 ± 73,000, and 748,000 ± 82,000 (mean ± SD) for 5.1 + 9.1, 5.1 + 6.1, and 6.1 + 9.1, respectively. The values of $\langle M\rangle_w$ measured by CLS and the average molecular weights estimated from EM data are summarized in Table III. The uncertainty in each of these values was estimated by propagation of error analysis (see footnote in Table III). $\langle M\rangle_w$ from both CLS and EM increased in the order 5.1 + 9.1 < 5.1 + 6.1 < 6.1 + 9.1. The estimates from EM data were always higher than from CLS. To determine if statistically significant differences existed between the estimates obtained by CLS and EM, and between the individual mAb pairs, the means were compared by computing the normal deviate (Z-statistic), and assuming that the individual estimates represented means of indefinitely large samples. The values of $\langle M\rangle_w$ obtained by CLS and EM for 5.1 + 6.1 and for 6.1 + 9.1 were not significantly different, nor were the values for 5.1 + 9.1 vs. 5.1 + 6.1 from EM. All other values (5.1 + 9.1 by CLS and EM, different mAb pairs by both EM and CLS) were significantly different at the $P = 0.05$ level.

Comparison of Size Parameters from Light Scattering and Electron Microscopy

To permit further quantitative comparison between the results obtained with QLS, CLS, and EM, we used the Porod-Kratky wormlike chain theory (24) to model the conformational behavior of the Ag-mAb complexes in solution. This model describes semiflexible chains in terms of a persistence length a which is a measure of chain stiffness. The model covers the range from random coils ($a \ll L$) to rigid rods ($a \gg L$).

Theoretical Relationships. The following analytical relationships for complexes containing i units were employed. For a wormlike linear chain, the mean square end-to-end distance $\langle R^2\rangle_i$ is related to the persistence length a and the contour length L_i by (24)

$$\langle R^2\rangle_i = 2aL_i\left(1 - \frac{a}{L_i}\left[1 - \exp\left(\frac{-L_i}{a}\right)\right]\right). \quad (11)$$

The mean-square radius of gyration $\langle R_g^2\rangle_i$ for a wormlike linear chain is related to the persistence length and the contour length by (25)

$$\langle R_g^2\rangle_i = \frac{1}{3}L_i a - a^2 + \frac{2a^3}{L_i} - \frac{2a^4}{L_i^2}\left[1 - \exp\left(\frac{-L_i}{a}\right)\right]. \quad (12)$$

A cycle is represented as a rigid disk, so that (26)

$$\langle R_g^2\rangle_i = \frac{1}{16}\left(\frac{L_i^2}{\pi^2} + d^2\right). \quad (13)$$

The hydrodynamic radius of a Porod-Kratky linear chain is a function of L_i, a, and d (the thickness of the chain) according to

$$R_{hi} = f_1(L_i, a, d). \quad (14)$$

Eq. 14 represents Eqs. 49–52 in reference 27. The hydrodynamic radius of wormlike rings is

$$R_{hi} = f_2(L_i, a, d), \quad (15)$$

which represents Eqs. 24–25 of reference 28. Thus, for any single linear Ag-mAb complex having i units, $\langle R^2\rangle_i$ and $\langle R_g^2\rangle_i$ are each a function of L_i and a, whereas R_{hi} is a function of L_i, a, and d. For a cycle, $\langle R_g^2\rangle_i$ is a function of L_i and d through use of Eq. 13.

The EM data, together with Eqs. 12–15, were employed to estimate overall values of z-average radius of gyration and hydrodynamic radius ($\langle R_g^2\rangle_z^{1/2}$ and $\langle R_h\rangle_z$) for each of the Ag-Ab complex systems using

$$\langle R_g^2\rangle_z^{1/2} = \left[\frac{\Sigma N_i M_i^2 \langle R_g^2\rangle_i}{\Sigma N_i M_i^2}\right]^{1/2} \quad (16)$$

$$\langle R_h\rangle_z = \left[\frac{\Sigma N_i M_i^2 (1/R_{hi})}{\Sigma N_i M_i^2}\right]^{-1}, \quad (17)$$

where the summation is carried out over both linear and cyclic chains.

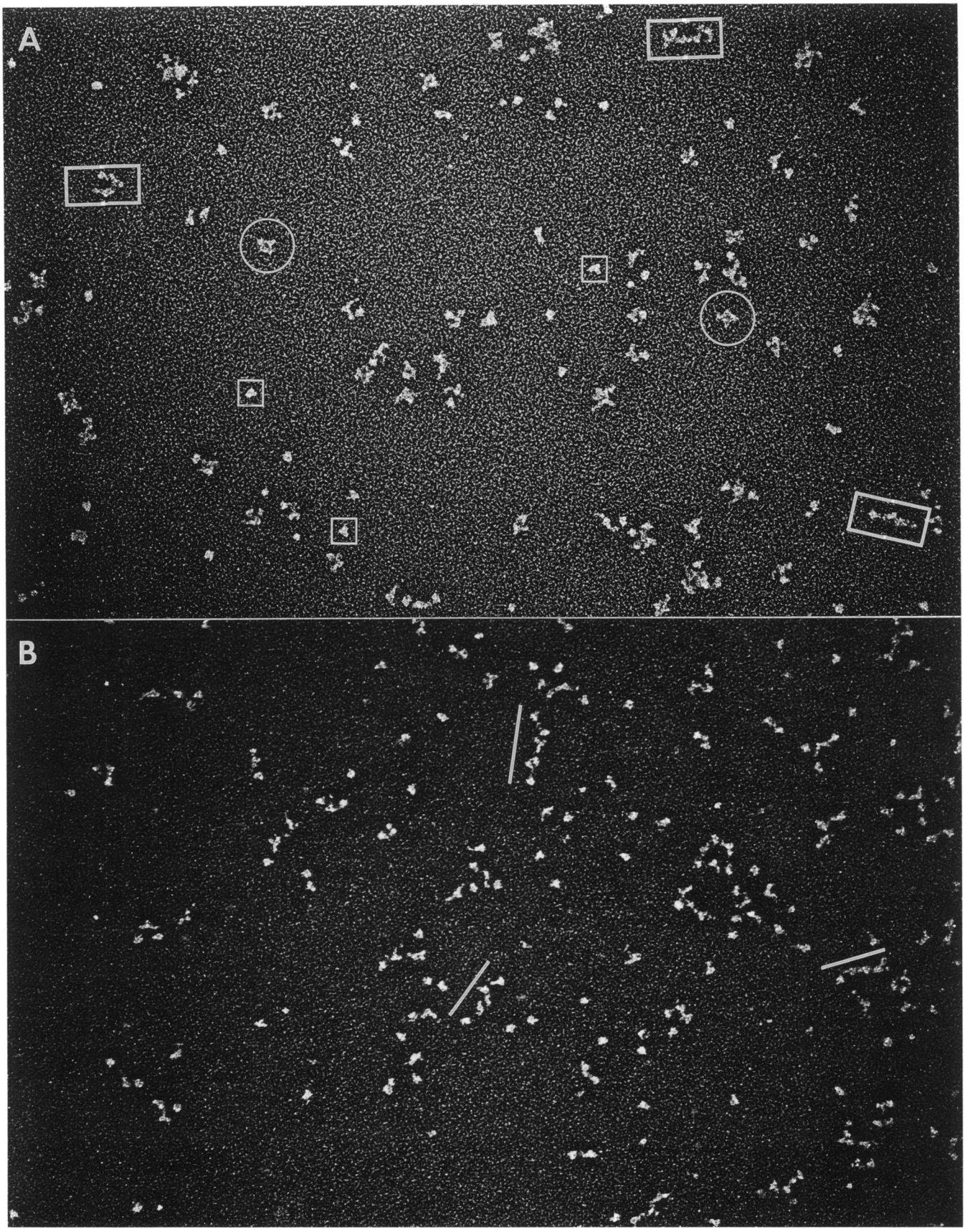

Figure 3 (Continued)

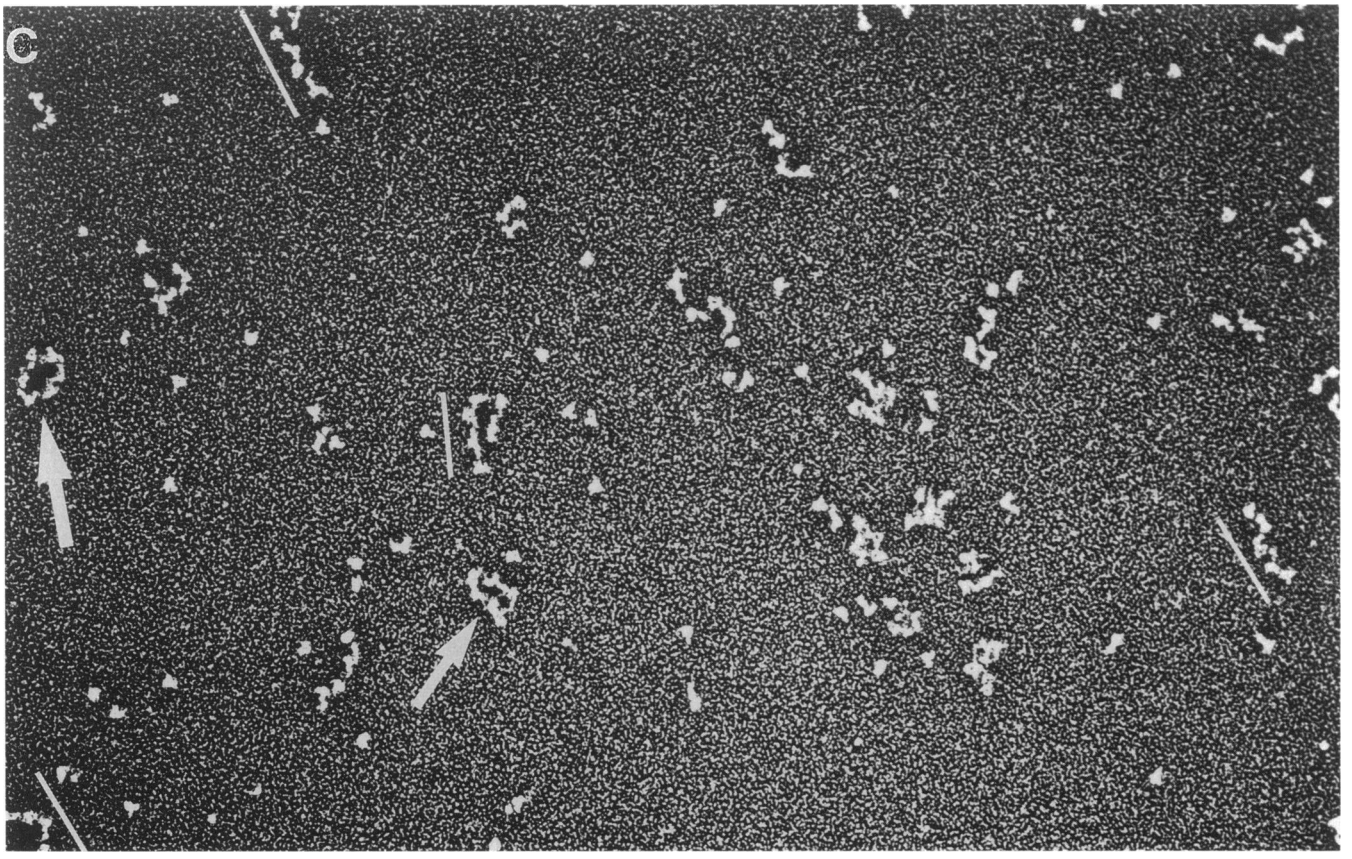

FIGURE 3 Darkfield electron photomicrograph of complexes of two mAb with BSA prepared by rotary coating with tungsten. (*A*) 5.1 + 9.1 + BSA. Representative structures are identified as follows: within squares, single antibody; circles, two-antibody cycles; rectangles, longer linear chains. (*B*) 5.1 + 6.1 + BSA. Structures underlined are longer linear chains. (*C*) 6.1 + 9.1 + BSA. Arrows point to four- and six-antibody cycles. Structures underlined are longer linear chains.

Results of Calculations. Two independent sets of calculations were employed with each mAb combination. In the first approach, the EM data alone were used to calculate $\langle R_g^2 \rangle_z^{1/2}$ for comparison with the value measured with CLS. To accomplish this, the persistence length a_i for each set of complexes of i units was calculated from the measured values of $\langle R^2 \rangle_i$ and L_i using Eq. 11. Individual values of a_i are summarized in Table IV. The number-average persistence length (mean ± SD), evaluated from data for complexes containing three or more units, was 200 ± 50 Å for 5.1 + 9.1, 470 ± 95 Å for 5.1 + 6.1, and 350 ± 110 Å for 6.1 + 9.1. Next, the values of L_i and a_i were used to estimate $\langle R_g^2 \rangle_i$ (Table IV) with Eq. 12 for open chains and Eq. 13 for cycles (with d = 100 Å). Use of this fixed value of d was justified by the results described below; furthermore, the final result was insensitive to the value of d selected. Lastly, the estimates of $\langle R_g^2 \rangle_i^{1/2}$ were used with Eq. 16 to estimate $\langle R_g^2 \rangle_z^{1/2}$. The final results, and the standard deviations estimated by propagation of error analysis, are summarized in Table II. Estimates of $\langle R_g^2 \rangle_z^{1/2}$ were uniformly higher from EM than from CLS, but the differences were not significantly different. $\langle R_g^2 \rangle_z^{1/2}$ for different mAb pairs increased in the same order as $\langle M \rangle_w$ (Table III); all differences were significant at the $P = 0.05$ level except for 5.1 + 6.1 vs. 6.1 + 9.1 by both CLS and EM. Similar calculations could not be carried out for $\langle R_h \rangle_z$ because it is sensitive to d, the value of which is unknown at this point.

In the second approach, Eqs. 12–17 were simultaneously solved by an iterative procedure using the EM data for N_i, M_i, and L_i to find the values of a and d which gave agreement between the prediction and the measured values of $\langle R_g^2 \rangle_z^{1/2}$ and $\langle R_h \rangle_z$ from light scattering. Because of the relative insensitivity of $\langle R_g^2 \rangle_z^{1/2}$ to the estimate of d, virtually the same results would be obtained by a sequential fitting procedure in which a is first evaluated with d fixed at 100 Å using Eqs. 12, 13, and 16, and then d is evaluated using Eqs. 14 and 17. The results of the analysis are shown graphically in Fig. 6. The single datum point in each plot represents the experimentally measured values of $\langle R_g^2 \rangle_z^{1/2}$ and $\langle R_h \rangle_z$ from which unique values of a and d are specified on each inset graph. Because of the small SD in $\langle R_h \rangle_z$, d is specified with high precision; by contrast, the error bars associated with $\langle R_g^2 \rangle_z^{1/2}$ lead to a relatively large uncertainty in the estimates of a. The best estimates of a and d (from the plots in the center row of Fig. 6) using the

TABLE IV
ANALYSIS OF ELECTRON MICROGRAPHS USING POROD-KRATKY MODEL

Component	No. of units (i) in Ag-mAb complex	No. of complexes N_i	Mol wt. $10^3\ M_i$	Contour length L_i	Root mean-square end-to-end distance $\langle R^2\rangle_i^{1/2}$	Persistence length a_i	Root mean-square radius gyration $\langle R_g^2\rangle_i^{1/2}$
5.1 + 9.1 + BSA				Å	Å	Å	Å
Open chains	1	374	220	190 ± 35	180 ± 110	1600	53 ± 12
	2	164	440	370 ± 85	290 ± 200	230 ± 700	93 ± 21
	3	127	660	530 ± 100	360 ± 270	170 ± 70	120 ± 21
	4	43	880	790 ± 120	530 ± 400	260 ± 80	180 ± 24
	5	18	1100	1030 ± 110	640 ± 490	270 ± 50	220 ± 20
	6	9	1320	1190 ± 240	650 ± 410	220 ± 70	230 ± 38
	7	5	1540	1220 ± 240	820 ± 420	410 ± 190	270 ± 51
	8	1	1760	1384	650	180 ± 17	240 ± 14
Closed cycles	2	186	440	470 ± 190	—	—	45 ± 6
	4	28	880	750 ± 140	—	—	65 ± 10
	6	2	1320	1070 ± 170	—	—	89 ± 13
5.1 + 6.1 + BSA							
Open chains	1	233	220	180 ± 45	180 ± 130	760	52 ± 14
	2	81	440	340 ± 75	320 ± 210	710	94 ± 22
	3	51	660	350 ± 120	460 ± 350	430 ± 460	140 ± 33
	4	22	880	830 ± 150	660 ± 440	510 ± 350	210 ± 36
	5	9	1100	1090 ± 140	760 ± 530	410 ± 140	250 ± 31
	6	4	1320	1240 ± 90	970 ± 450	740 ± 190	310 ± 21
	7	1	1540	1660	1290	950 ± 210	410 ± 25
	8	1	1760	1480	1130	800 ± 180	360 ± 24
Closed cycles	2	4	440	440 ± 80	—	—	43 ± 5
	4	2	880	970 ± 110	—	—	81 ± 8
	6	1	1320	1460 ± 100	—	—	119 ± 8
6.1 + 9.1 + BSA							
Open chains	1	272	220	170 ± 40	180 ± 110	—	48 ± 11
	2	86	440	350 ± 100	330 ± 240	990	98 ± 31
	3	62	660	620 ± 150	490 ± 360	380 ± 360	150 ± 37
	4	25	880	890 ± 150	610 ± 470	320 ± 130	200 ± 32
	5	27	1100	1170 ± 240	690 ± 590	260 ± 90	240 ± 42
	6	12	1320	1300 ± 170	760 ± 660	290 ± 70	260 ± 31
	7	11	1540	1600 ± 240	910 ± 770	320 ± 80	320 ± 41
	8	0	1760	—	—	—	—
	9	3	1980	2000 ± 700	1500 ± 1200	1050 ± 390	490 ± 140
Closed cycles	2	10	440	380 ± 100	—	—	39 ± 6
	4	17	880	1040 ± 140	—	—	86 ± 11
	6	5	1320	1470 ± 150	—	—	120 ± 12

N_i, M_i, L_i, and $\langle R^2\rangle_i$ were measured from electron photomicrographs as described in the text. Persistence length a_i was calculated from Eq. 11. $\langle R_g^2\rangle_i$ was calculated from Eq. 12 for all open linear chains, and from Eq. 13 for closed cycles. $\langle R_g^2\rangle_z^{1/2}$ was calculated from this data using Eq. 16. SD for L_i and $\langle R^2\rangle_i^{1/2}$ were calculated from the raw data. The latter quantity is much larger than measurement error and reflects the distribution of end-to-end distances. For a_i and $\langle R_g^2\rangle_{iz}^{1/2}$, SD were estimated by propagation of error analysis. For this purpose, the error in the measurement of the root-mean-square end-to-end distance was estimated to be ±40 Å.

data in Table IV are a = 91 Å and d = 85 Å for 5.1 + 9.1, a = 430 Å and d = 83 Å for 5.1 + 6.1, and a = 205 Å and d = 110 Å for 6.1 + 9.1. These estimates of persistence length from Fig. 6 are uniformly lower than the values obtained in the first approach using EM data alone. However, in all cases, the maximum extrema (mean + SD) represented by the error bars in the upper plots overlap the minimum extrema (mean − SD) from the first set of estimates, thus suggesting that the differences in the estimates from the two approaches are not statistically significant. The differences between mAb combinations is consistent in both calculation methods in that the persistence length increases in the order 5.1 + 9.1 < 6.1 + 9.1 < 5.1 + 6.1.

Contributions to $\langle R_g^2\rangle_z$ and $\langle Rh\rangle_z$. The fitted values of a and d from the second approach described above, together with Eqs. 12–17 and the EM data (Table IV), were used to estimate the fractional contribution of each set of complexes containing i units to the measured values of $\langle R_g^2\rangle_z$ and $\langle R_h\rangle_z$. The results are shown in Fig. 7. $\langle R_h\rangle_z$ is determined primarily by the smaller components ($i \leqq 5$) in the complexes studied, and a substantial fraction of the

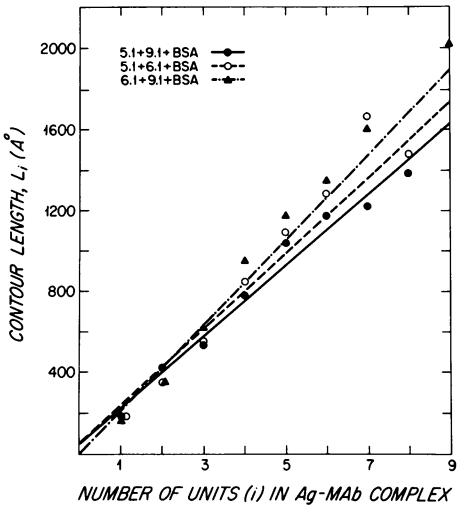

FIGURE 4 Contour length of complexes as a function of the number of Ag-mAb units, as measured from electron photomicrographs. Data for each mAb pair was fit by linear regression.

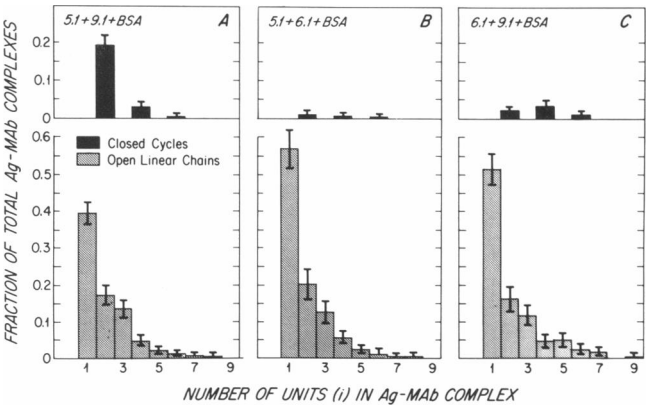

FIGURE 5 Frequency distributions of number of units (i) in Ag-mAb complexes, as determined from electron photomicrographs. (A) 5.1 + 9.1 + BSA. (B) 5.1 + 6.1 + BSA. (C) 6.1 + 9.1 + BSA. Error bars represent 95% confidence limits computed from Eq. 7 with $b = 1.96$.

measured value is contributed by complexes with $i = 1$ or 2, including cycles when present. By contrast, $\langle R_g^2 \rangle_z$ is insensitive to these small complexes ($i = 1$ or 2) and to cycles of almost any size, with the preponderant contributions arising from larger open linear chains ($i \geq 3$).

DISCUSSION

In a previous study using QLS to investigate the size of the Ag-mAb complexes (8), we found that the size of the complexes increased in the order 5.1 + 9.1 < 5.1 + 6.1 < 6.1 + 9.1. In this study, a more detailed characterization of the size, structure, and polydispersity of the same Ag-mAb complexes was undertaken. Three complementary techniques were used. $\langle R_h \rangle_z$ was determined with QLS, $\langle M \rangle_w$, and $\langle R_g^2 \rangle_z^{1/2}$ were measured with CLS, and detailed information regarding the molecular weight distribution, the presence of cycles or open chains, the contour length, and the end-to-end distance was obtained with EM. From this data, the contour length of a single Ag-mAb unit was calculated, and $\langle M \rangle_w$ was estimated for comparison with the values from CLS. The Porod-Kratky wormlike chain theory was used to model the conformation of the Ag-mAb complexes. The persistence length a was estimated using this model from the EM data and these results, together with an estimate of the hydrodynamic thickness d, were then used to estimate $\langle R_g^2 \rangle_z$ for comparison with the CLS results. In addition, the same theory was used to find the values of a and d which gave agreement between the CLS and QLS measurement and the predictions based upon the EM data. Lastly, these results and the conformation model were used to estimate the contributions of the individual Ag-mAb complexes to the measured values of $\langle R_h \rangle_z$ and $\langle R_g^2 \rangle_z^{1/2}$.

Ag-mAb complexes prepared from the three different mAb pairs displayed significantly different properties as assessed by each of the techniques employed. Measurements of mean size by three different techniques ($\langle R_h \rangle_z$ by

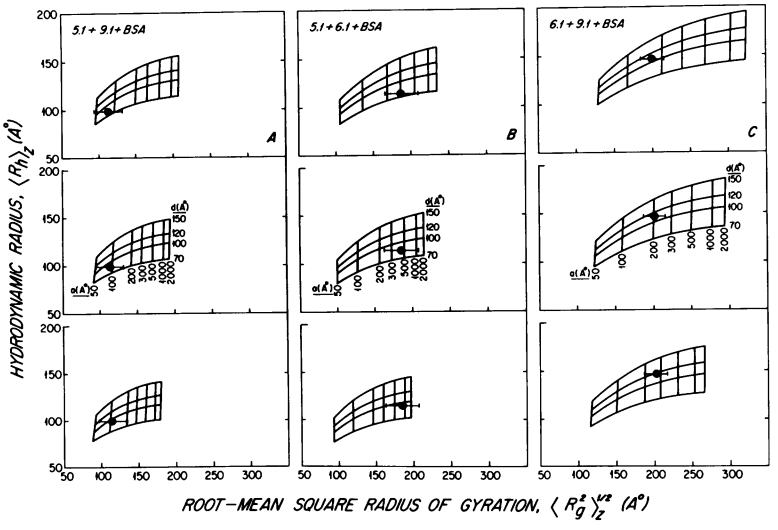

FIGURE 6 Relationship between $\langle R_g^2 \rangle_z^{1/2}$, $\langle R_h \rangle_z$, persistence length, a, and chain thickness, d. Calculations were carried out using the Porod-Kratky wormlike chain model and the data for N_i, M_i, and L_i derived from the electron photomicrographs. (A) 5.1 + 9.1 + BSA. (B) 5.1 + 6.1 + BSA. (C) 6.1 + 9.1 + BSA. Error bars represent ±SD in measurement of $\langle R_g^2 \rangle_z^{1/2}$. Error bars for $\langle R_h \rangle_z$ are contained within each datum point. In each plot, a single combination of $\langle R_g^2 \rangle_z^{1/2}$ and $\langle R_h \rangle_z$ uniquely specifies a single combination of a and d as shown in the inset. The inset graphs in the center row correspond to the mean values of the parameters in Table IV. The inset graphs in the upper and lower plots are model calculations corresponding to the extremes in the uncertainty (±SD) of the component values of $\langle R_g^2 \rangle_i$ associated with the uncertainty in N_i, M_i, and L_i as assessed by propagation of error analysis.

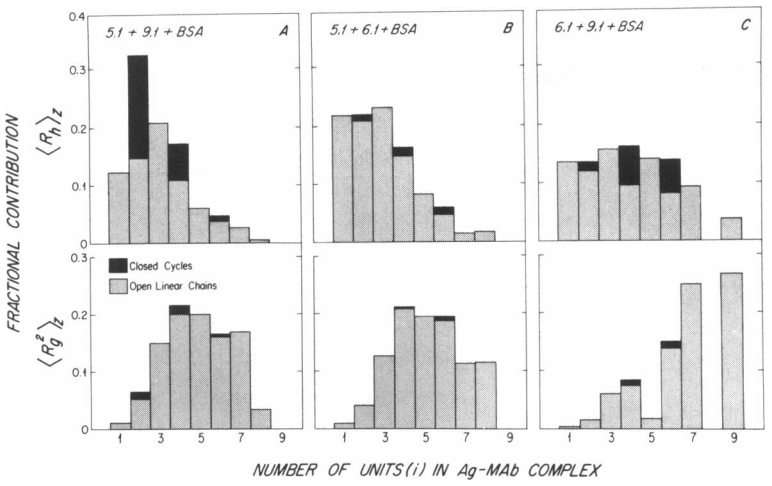

FIGURE 7 Estimated fractional contribution of each set of complexes containing i units to measured values of $\langle R_g^2 \rangle_z$ and $\langle R_h \rangle_z$. (*A*) 5.1 + 9.1 + BSA. (*B*) 5.1 + 6.1 + BSA. (*C*) 6.1 + 9.1 + BSA. Stippled bars show contribution from open linear chains. Solid bars indicate additional contribution from closed cycles.

QLS, $\langle R_g^2 \rangle_z^{1/2}$ by CLS, $\langle M \rangle_w$ by CLS and EM) confirmed our earlier finding with $\langle R_h \rangle_z$ measurements (8) that mean size increased in the order 5.1 + 9.1 < 5.1 + 6.1 < 6.1 + 9.1. The ratio $\langle R_h \rangle_z / \langle R^2_g \rangle_z^{1/2}$ decreased from 0.87 to 0.61 in the order 5.1 + 9.1 > 6.1 + 9.1 > 5.1 + 6.1. The value of this ratio is 0.27 for a long rigid rod, 0.71 for a disk, 0.875 for a random coil, and 1.29 for a compact sphere (29). Although exact interpretation of these values for polydisperse systems of the type we studied is difficult, the qualitative trend we observed suggests a change from a more compact structure for 5.1 + 9.1 to more extended structures for 6.1 + 9.1 and 5.1 + 6.1.

Observations from EM photomicrographs were consistent with the results from light scattering and demonstrated further differences in size distribution and solution conformation. In particular, two-antibody cyclic complexes were abundant with 5.1 + 9.1 but with no other mAb pair; a smaller proportion of four- and six-antibody cycles were present with 6.1 + 9.1, and virtually no cycles occurred with 5.1 + 6.1. Values of $\langle R^2 \rangle_i$ for linear chains measured on the photomicrographs increased in the order 5.1 + 9.1 < 6.1 + 9.1 < 5.1 + 6.1. Estimates of persistence lengths evaluated from this data using the Porod-Kratky model, as well as values estimated by fitting EM data to the light scattering results, also increased in the same order. Because persistence length is a measure of chain stiffness, these results indicate that chain flexibility decreased in the order 5.1 + 9.1 > 6.1 + 9.1 > 5.1 + 6.1.

The differences observed between the mAb pairs would not have been expected on the basis of predictions of idealized thermodynamic models, which either neglect (7) or include (30, 31) cycle formation. These models construct an equilibrium size distribution of linear chains or closed cycles from bivalent antibodies and antigens, in which the growth of complexes is based on the intrinsic association constant between a single antibody and antigen. For example, the association constant K_a of both 5.1 and 9.1 to BSA is nearly identical, yet 6.1 + 9.1 yielded larger chains and had a greater propensity to form cycles than 5.1 + 6.1. Furthermore, K_a for 5.1 is about sixfold higher than for 6.1, yet 5.1 + 9.1 was much smaller than 6.1 + 9.1 and formed many small cycles which, in part, contributed to its smaller size. In contrast to its lack of correlation with the magnitude of K_a, the extent of cycle formation correlated strongly with the flexibility of the linear chains. The mAb pair 5.1 + 9.1 displayed the most flexible chains and the highest $\langle R_h \rangle_z / \langle R^2_g \rangle_z^{1/2}$ ratio, and was the only mAb pair to form large numbers of small, two-antibody cycles. In contrast, 5.1 + 6.1 was the stiffest, formed the most extended chains, and was virtually unable to form cycles; 6.1 + 9.1 was intermediate in stiffness and was able to form larger four- and six-antibody cycles but relatively fewer two-antibody cycles. The exact origin of these differences is unknown; we suggest that they result from steric constraints imposed by the three-dimensional topography of the individual epitopes and/or their environment as well as the relative epitope locations on BSA.

Several lines of evidence suggest that the quantitative results obtained by analysis of the EM photomicrographs provide a reasonable representation of the Ag-mAb complexes in solution. First, the contour length of a single Ag-mAb unit, which ranged from 190 to 205 Å, is comparable to the values one would estimate from known molecular dimensions. The Fab arm is ~65 Å long and 35 Å wide (32). The distance between the two binding sites on each mAb therefore ranges from ~90 Å at a 90° range angle to ~130 Å at a 180° angle. BSA at physiological pH appears on photomicrographs as an oblate ellipsoid with a major axis of 60 Å and a minor axis of 45 Å (22). Thus, the length of one Ag-mAb complex would range from ~90 + 45 = 135 Å to ~130 + 60 = 190 Å. Second, $\langle M \rangle_w$ estimated from the EM data agreed well with the values from CLS in two of the three cases. For only one mAb pair, 5.1 + 9.1, were the results significantly different at the P = 0.05 level. Third, the values of $\langle R_g^2 \rangle_z^{1/2}$ estimated from EM data were not significantly different from those measured by CLS in all three cases. Nonetheless, both size estimates from EM data were always higher than the comparable

values measured by CLS, suggesting a modest systematic error in the EM data. Possible sources of this error include inadvertent operator bias in selection of too few small complexes, aggregation during processing, and statistical overlap of some nonassociated AG-mAb complexes, which was observed to a small extent in the control sample (9.1 + BSA). Possible compensating phenomena which would lead to smaller complex sizes include shear-induced fragmentation during spraying (33), disruption of surface tension forces during sample drying (20), and neglect of some larger poorly defined complexes. Lastly, the values of $\langle R^2 \rangle_i$ measured in two dimensions on the photomicrographs, from which values of persistence length were estimated, may not represent the true value in solution because of conformational changes upon attachment to the surface or during sample drying.

The Porod-Kratky model was used to model the conformational behavior of the Ag-mAb complexes, although it is more typically used for macromolecules having larger L/d ratios, such as DNA strands (34). Models which describe thick, semiflexible chains are not available to our knowledge. Other simpler constructs could have been used, such as cylinders, sliding rods, or weakly bending rods (17, 26, 35). However, because a significant number of complexes did not appear rigid on EM, and because the hinge flexibility of antibodies is well-documented (36), we chose not to model the complexes as rigid shapes. A source of error in applying the wormlike model to short complexes derives from the neglect of chain thickness. For example, for complexes of two Ag-mAb units, the model for rigid cylinders of finite thickness (assumed to be 100 Å) predicts a radius of gyration 20% higher than the Porod-Kratky estimate. However, any error in $\langle R_g^2 \rangle_i^{1/2}$ and R_{hi} for small complexes attributable to neglect of the chain thickness is overwhelmed by the z-averaging, because longer complexes are more heavily weighted in determining $\langle R_g^2 \rangle_z^{1/2}$ and $\langle R_h \rangle_z$, the quantities measurable by light scattering. The model for determining R_{hi} also neglects end effects (37). However, it has recently been shown that end effects are negligible down to a L/d ratio ~4 and contribute only 18% to R_h even at $L/d \sim 1$ (36). Notwithstanding these problems, the size parameters obtained by employing the Porod-Kratky model show good agreement with those obtained by light scattering (Table II).

Electron microscopy has been previously employed in several studies of Ag-Ab complexes. Early work (36, 38) involved studies of anti-hapten complexes. More recently, EM has been used in studies of Fc-mediated precipitation (39), the segmental flexibility of Fab arms (40), and idiotope mapping (41). Most previous investigations have used negative staining, in contrast to the shadowcasting technique used in this study. In one case (9.1 + 6.1 + BSA), we did prepare and examine a negatively-stained specimen. The results showed far fewer long linear chains and many more two-antibody cycles in the negatively stained micrograph (data not shown) than that observed with the shadowcasting technique. A possible explanation for this marked difference is that the lower pH of the uranyl acetate stain (4.5–5.5) altered the complexes by disruption of Ag-Ab bonds (42) and/or by BSA conformational changes which are known to occur at pH 4–4.5 (22, 43). Thus, the rotary-shadowcasting technique was used in this study to obtain a more accurate representation of the true complex distribution.

This detailed characterization of size and shape of Ag-Ab complexes is an important first step towards understanding how these parameters affect the size and structure of more complex Ag-Ab systems. Further investigations will eventually provide information on the importance of complex size and structure on subsequent binding and processing events such as complement activation, phagocytosis, and overall clearance from the circulation.

We gratefully acknowledge Professor George Benedek who kindly provided access to the light scattering apparatus located in his laboratory in the Department of Physics at MIT.

This work was supported in part by National Institutes of Health Grants CA 45272 and CA 33956 and by National Science Foundation Grant PCM 8313025. Martin L. Yarmush is a Lucille P. Markey Scholar in Biomedical Science.

Received for publication 8 October 1987 and in final form 8 February 1988.

REFERENCES

1. Brennan, F. M., S. A. Grace, and C. J. Elson. 1983. Preparation of covalent IgG complexes of defined size and their clearance from the circulation of mice. *J. Immunol. Methods.* 56:149–158.
2. Segal, D. M., S. K. Dower, and J. A. Titus. 1983. The FcR-mediated endocytosis of model immune complexes by cells from the P333D mouse macrophage line. *J. Immunol.* 130(Suppl. 1):130–137.
3. Plotz, P. H., R. P. Kimberly, R. L. Guyer, and D. M. Segal. 1979. Stable model immune complexes produced by bivalent affinity labelling haptens in-vivo survival. *Mol. Immunol.* 19:99–110.
4. Doekes, G., L. A. van Es, and M. R. Daha. 1984. Binding and activation of the first complement component by soluble immune complexes: effect of complex size and composition. *Scand. J. Immunol.* 19:99–110.
5. Arend, W. P., D. C. Teller, and M. Mannik. 1972. Molecular composition and sedimentation characteristics of soluble antigen-antibody complexes. *Biochemistry.* 11:4063–4072.
6. Kijlstra, A., D. W. Knutson, A. van der Lielig, and L. A. van Es. 1977. Characteristics of soluble immune complexes prepared from oligovalent DNP conjugates and anti-DNP antibodies. *J. Immunol. Methods.* 17:263–277.
7. Steensgard, J., C. Jacobsen, J. Lowe, N. R. Ling, and R. Jefferis. 1982. Theoretical and ultracentrifugal analysis of immune complex formation between monoclonal antibodies and human IgG. *Immunology.* 46:751–760.
8. Yarmush, D. M., R. M. Murphy, C. K. Colton, M. Fisch, and M. L. Yarmush. 1988. Quasi-elastic light scattering of antigen-antibody complexes. *Mol. Immunol.* 25:17–25.
9. Morel, G. A., D. M. Yarmush, C. K. Colton, D. C. Benjamin, and M. L. Yarmush. 1988. Monoclonal antibodies to bovine serum albumin: affinity and specificity determination. *Mol. Immunol.* 25:7–16.
10. Yarmush, D. M., G. A. Morel, and M. L. Yarmush. 1987. A new technique for mapping epitope specificities of monoclonal anti-

bodies using quasielastic light scattering spectroscopy. *J. Biochem. Biophys. Methods.* 14:279–289.
11. Kohn, J., and M. Wilchek. 1984. The use of cyanogen bromide and other novel cyanylating agents for the activation of polysaccharide resins. *Appl. Biochem. Biotech.* 9:285–305.
12. Haller, H. R., C. Destor, and D. S. Cannell. 1983. Photometer for quasi-elastic and classical light scattering. *Rev. Sci. Instrum.* 54:973–983.
13. Bender, T. M., R. J. Lewis, and R. Pecora. 1986. Absolute Rayleigh ratios of four solvents at 488 nm. *Macromolecule.* 19:244–245.
14. Geiduschek, E. P., and A. Holtzer. 1958. Application of light scattering to biological systems: deoxyribonucleic acid and the muscle proteins. *Adv. Biol. Med. Phys.* 6:431–551.
15. Huglin, M. B. 1972. Light Scattering from Polymer Solutions. Academic Press, New York. 165–331.
16. Koppel, D. E. 1972. Analysis of macromolecular polydispersity in intensity correlation spectroscopy: the method of cumulants. *J. Chem. Phys.* 57:4814–4820.
17. Schmidt, M., and W. H. Stockmayer. 1984. Quasi-elastic light scattering by semiflexible chains. *Macromolecule.* 17:509–514.
18. Slayter, H. S. 1976. High resolution metal replication of macromolecules. *Ultramicroscopy.* 1:341–357.
19. Chung, K. L. 1974. Elementary Probability Theory with Stochastic Processes. Springer-Verlag, New York.
20. Flory, P. J. 1953. Principles of Polymer Chemistry. Cornell University Press, Ithaca, NY.
21. Galvin, N. J., V. M. Dixit, K. M. O'Rourke, S. A. Santaro, G. A. Grant, and W. A. Frazier. 1985. Mapping of epitopes for monoclonal antibodies against human platelet thrombospondin with electron microscopy and high sensitivity amino acid sequencing. *J. Cell Biol.* 101:1434–1441.
22. Slayter, E. M. 1965. An electron microscope study of the conformational change in bovine serum albumin at low pH. *J. Mol. Biol.* 14:443–452.
23. Fasman, G. D., ed. 1976. Handbook of Biochemistry and Molecular Biology. CRC Press, Boca Raton, FL.
24. Cantor, C. R., and P. R. Schimmel. 1980. Biophysical Chemistry. W. H. Freeman and Co., San Francisco.
25. Benoit, H. P., and P. Doty. 1953. Light scattering from branched polymers and biopolymers. *J. Phys. Chem.* 57:958–963.
26. Burchard, W. 1983. Static and dynamic light scattering from branched polymers and biopolymers. *Adv. Polym. Sci.* 48:4–124.
27. Yamakawa, H., and M. Fujii. 1973. Translational friction coefficient of wormlike chains. *Macromolecule.* 6:407–415.
28. Fujii, M., and H. Yamakawa. 1975. Moments and transport coefficients of wormlike rings. *Macromolecule.* 8:792–799.
29. Slayter, H., J. Loscalzo, P. Bockenstedt, and R. I. Handin. 1985. Native conformation of human von Willebrand protein. *J. Biol. Chem.* 260:8559–8563.
30. Archer, B. G., and H. Krakauer. 1977. Thermodynamics of antibody-antigen reactions. *Biochemistry.* 16:615–627.
31. Moyle, W. R., C. Lin, R. L. Corson, and P. H. Ehrlich. 1983. Quantitative explanation for increased affinity shown by mixtures of monoclonal antibodies: importance of a circular complex. *Mol. Immunol.* 20:439–452.
32. Green, N. M. 1969. Electron microscopy of the immunoglobulins. *Adv. Immunol.* 11:1–30.
33. Mould, A. P., D. F. Holmes, K. E. Kadler, and J. A. Chapman. 1985. Mica sandwich technique for preparing macromolecules for rotary shadowing. *J. Ultrastruct. Res.* 91:66–76.
34. Jolly, D., and H. Eisenberg. 1976. Photon correlation spectroscopy, total intensity light scattering with laser radiation, and hydrodynamic studies of well-fractionated DNA sample. *Biopolymers.* 15:61–95.
35. Zero, K., and R. Pecora. 1982. Restricted flexing at once-broken rods. *Macromolecule.* 15:1023–1027.
36. Valentine, R. C., and N. M. Green. 1967. Electron microscopy of an antibody-hapten complex. *J. Mol. Biol.* 27:615–617.
37. Norisuye, T., M. Motowoka, and H. Fujita. 1979. Wormlike chains near the rod limit: translational friction coefficient. *Macromolecule.* 12:320–323.
38. Schumaker, V. N., G. W. Seegan, C. A. Smith, S. K. Ma, J. D. Rodwell, and M. F. Schumaker. 1980. The free energy of angular position of the Fab arms of IgG antibody. *Mol. Immunol.* 17:413–423.
39. Moller, N. P. H., and G. Christiansen. 1983. Fc-mediated immune precipitation. III. Visualization by electron microscopy. *Immunology.* 48:469–476.
40. Wrigley, N. G., E. B. Brown, and J. J. Skehel. 1983. Electron microscopic evidence for the axial rotation and inter-domain flexibility of the Fab regions of immunoglobulin G. *J. Mol. Biol.* 169:771–774.
41. Roux, K. H., and D. W. Metzger. 1982. Immunoelectron microscopic localization of idiotypes and allotypes on immunoglobulin molecules. *J. Immunol.* 129:2548–2553.
42. Singer, S. J., and D. H. Campbell. 1955. Physical chemical studies of soluble antigen-antibody complexes. IV. The effect of pH on the reaction between bovine serum albumin and its rabbit antibodies. *J. Am. Chem. Soc.* 77:3504–3510.
43. Peters, T. 1985. Serum albumin. *Adv. Protein Chem.* 37:161–245.